Check for updates

Deep tissue multi-photon imaging using adaptive optics with direct focus sensing and shaping

Zhongya Qin[1,7], Zhentao She [1,7], Congping Chen[1], Wanjie Wu [1], Jackie K. Y. Lau[2,3,4,5], Nancy Y. Ip[2,3,4,5,6] and Jianan Y. Qu [1,3,4] ✉

High-resolution optical imaging deep in tissues is challenging because of optical aberrations and scattering of light caused by the complex structure of living matter. Here we present an adaptive optics three-photon microscope based on analog lock-in phase detection for focus sensing and shaping (ALPHA-FSS). ALPHA-FSS accurately measures and effectively compensates for both aberrations and scattering induced by specimens and recovers subcellular resolution at depth. A conjugate adaptive optics configuration with remote focusing enables in vivo imaging of fine neuronal structures in the mouse cortex through the intact skull up to a depth of 750 μm below the pia, enabling near-non-invasive high-resolution microscopy in cortex. Functional calcium imaging with high sensitivity and high-precision laser-mediated microsurgery through the intact skull were also demonstrated. Moreover, we achieved in vivo high-resolution imaging of the deep cortex and subcortical hippocampus up to 1.1 mm below the pia within the intact brain.

Breakthroughs in imaging technology have been the primary driving force of new biological discoveries. Optical microscopy has greatly facilitated biomedical research in recent decades, with its ability to provide structural and functional information in living specimens at high spatiotemporal resolution. However, optical aberration and scattering occur as light travels through and interacts with inhomogeneous biological tissues, such as the mammalian brain, fundamentally limiting the performance of optical microscopy in both resolution and depth.

Multi-photon microscopy, which is the current method of choice for in vivo brain imaging of small animals, alleviates the scattering issue by selectively exploiting the ballistic (unscattered) photons for excitation[1,2]. Recently, three-photon microscopy has shown great potential to extend the imaging depth by using longer wavelength and higher-order non-linear excitation to reduce the scattering further and suppress the unwanted background fluorescence[3,4]. However, 3PM still suffers from aberrations arising from the variations of refractive index in biological tissues, preventing the ballistic photons from forming a diffraction-limited focus and heavily degrading the spatial resolution[5]. This ultimately prohibits in vivo multi-photon imaging being used to resolve subcellular structures in the deep cortical and subcortical layers in a minimally invasive manner. Adaptive optics (AO) compensation of specimen-induced aberrations is essential to recover optimal imaging performance at depth[6,7]. The desired excitation wavefront can be determined using either direct[8–10] or indirect[11–14] approaches. Direct wavefront sensing of a fluorescent guide star inside biological tissue enables rapid measurement of aberration, but it depends on quasi-ballistic photons for wavefront sensing, and the performance degrades rapidly at depth[9,10]. In indirect sensing approaches, various algorithms are designed to determine the optimal corrective wavefront. The methods are more suitable for opaque tissues but are usually

time-consuming and mainly deal with optical aberrations[11,12]. Recently, an AO technique called focus scanning holographic aberration probing (F-SHARP) was developed to correct both aberrations and scattering at high speed in vivo[15,16]. F-SHARP measures the aberrated electric-field point spread function (E-field PSF) directly by using two-beam interference and compensates for the aberrations using phase conjugation of the measured PSF[17].

In this work, we developed an AO three-photon microscope (3PM) based on a method termed ALPHA-FSS, or α-FSS. The method shares the basic physical principle as F-SHARP technology and allows accurate measurement and corrective updates of both aberrations and scattering in highly turbid tissue at great depth. Specifically, α-FSS makes use of two innovations: direct focus sensing with phase-sensitive detection and conjugate AO with remote focusing. We introduced a high-frequency modulation and phase-sensitive detection scheme to achieve accurate measurement of the E-field PSF in a fast and photon-efficient manner, which allows subsequent aberration correction of a large number of modes by using a high-pixel-count wavefront corrector. In addition, we integrated a remote focusing approach with the conjugate AO configuration to enable effective single correction over a large volume for imaging through a turbid layer, such as intact skull of living mouse. Using this conjugate α-FSS–3PM technology, we first validated its imaging performance through the intact skull of mouse for both in vitro and in vivo preparations and achieved high spatial resolution with a substantially improved fluorescence signal over a large depth. We then applied it to in vivo structural and functional imaging of mouse cortices through the intact skull, which is desirable in the study of brain functions and diseases[18,19]. Taking advantage of the tight focus provided by α-FSS, we demonstrated precise laser microsurgery and investigated the subsequent microglial dynamics in cortex through the intact skull. Furthermore,

[1]Department of Electronic and Computer Engineering, The Hong Kong University of Science and Technology, Kowloon, Hong Kong, China. [2]Division of Life Science, The Hong Kong University of Science and Technology, Kowloon, Hong Kong, China. [3]State Key Laboratory of Molecular Neuroscience, The Hong Kong University of Science and Technology, Kowloon, Hong Kong, China. [4]Molecular Neuroscience Center, The Hong Kong University of Science and Technology, Kowloon, Hong Kong, China. [5]Hong Kong Center for Neurodegenerative Diseases, Hong Kong, China. [6]Guangdong Provincial Key Laboratory of Brain Science, Disease and Drug Development, HKUST Shenzhen Research Institute, Shenzhen-Hong Kong Institute of Brain Science, Shenzhen, China. [7]These authors contributed equally: Zhongya Qin, Zhentao She. ✉e-mail: eequ@ust.hk

by using a pupil α-FSS–3PM, we achieved high-resolution deep imaging of subcortical structures up to 1.1 mm below pia within the intact brain.

Results

Conjugate AO 3PM system based on α-FSS. Our conjugate α-FSS–3PM system consists of three key modules—that is, direct focus sensing, conjugate AO and remote focusing modules, as shown in Fig. 1a and Supplementary Fig. 1. The system aberrations are corrected by the deformable mirror (DM) using a simple sensorless AO method (Methods). The direct focus sensing in tissue is based on a phase-modulation and lock-in detection scheme (see details in Supplementary Information, 'Principle of α-FSS'). To measure the scattered and aberrated E-field PSF, a weak scanning beam raster scanned over a small field of view (FOV) is introduced to interfere with a strong stationary beam. Thus, the three-photon (3P) excited fluorescence signal at scanning coordinate x is given by:

$$I(x) \propto \int O(x') \left| E_{stat}(x') + E_{scan}(x'-x) \right|^6 dx' \qquad (1)$$

where E_{stat} and E_{scan} are the complex-valued E-field PSF of the stationary and scanning beam, and $O(x')$ is the real-valued object function related to the fluorophore distribution in the focal plane. By modulating the phase of the scanning beam at a fixed frequency ω and setting the scanning beam to be much weaker than the stationary beam (that is, $|E_{scan}|^2/|E_{stat}|^2 < 0.1$), the fluorescence signal $I(x,t)$ can be demodulated using a lock-in amplifier at frequency ω, outputting the orthogonal X (that is, in-phase) and Y (that is, quadrature). We may then compute the E-field PSF as

$$E_f(x) = X + jY \propto \underbrace{\int O(x') \left| E_{stat}(x') \right|^4 E_{stat}^*(x')}_{\delta-\text{like function}} E_{scan}(x'-x) dx'$$

$$(2)$$

Owing to the high sensitivity provided by our phase modulation and lock-in detection, the E-field PSF can be determined reliably by scanning a single frame of the FOV, regardless of the large DC background from the stationary beam. By measuring the aberrated E-field PSF, the desired corrective wavefront can be derived by using phase conjugation of the measured PSF. Then, a high-pixel-count spatial light modulator (SLM) acting as the wavefront corrector is employed to correct the aberrations over a large number of modes[15,16].

To evaluate the efficacy of our α-FSS–3PM and characterize its performance in through-skull imaging, we first conducted an in vitro experiment by imaging fluorescent beads embedded in agarose below an excised intact skull. To measure the wavefront distortions, the strong beam was parked at the brightest regions—for example, the center of fluorescent bead— whereas the weak beam was used to scan over a 16 × 16-μm² FOV to capture the complex E-field PSF. The overall aberrations can then be accurately determined and effectively corrected by using the two-dimensional Fourier transform of the measured E-field PSF, in a fast manner with only 2–3 iterations (Supplementary Fig. 2). As can be seen, the fluorescent bead image recorded with system aberration correction only is highly distorted, and the appearance of the side lobes indicates the high-order aberrations induced by the thick skull (Fig. 1b). In contrast, by applying the corrective phase pattern to the SLM to compensate for specimen-induced aberrations (Fig. 1c), we effectively recovered high imaging resolution, and improved the fluorescence intensity more than 200-fold (Fig. 1b,d). Note that the diffraction-limited resolution was not fully restored, likely due to the remaining uncorrected scattering.

In AO microscope systems, the wavefront corrector is usually projected to the rear pupil plane of the objective (Supplementary Fig. 3a). This convenient configuration, known as pupil AO, is implemented in almost all AO microscopes. However, pupil AO correction can restore the focus quality over only a very small FOV (<30 μm in diameter), as shown in Fig. 1e, because of the rapid decorrelation between the scanned corrective wavefront and the turbid skull with a highly heterogeneous distribution of refractive index. Because the mouse skull is the dominant aberration layer and accounts for most of the deterioration in transcranial brain imaging at depth, the effective FOV after AO correction can, in principle, be enlarged by conjugating the wavefront corrector to the skull layer, instead of the objective pupil plane. This approach, called conjugate AO, has been demonstrated to increase the corrective FOV in transcranial brain imaging in vivo[16,20]. However, these previous implementations of conjugate AO still have a limited axial FOV. To achieve a large effective imaging volume with a single AO correction, we integrated conjugate AO with remote focusing to maintain the conjugation between wavefront corrector and skull layer during axial sectioning[21]. Here, a fast electrical tunable lens (ETL) was used for axial scanning, and the aberrations induced by remote focusing are counted as part of system aberrations and corrected by the DM before α-FSS AO corrections (Methods). We measured the axial resolution of remote focusing as a function of focal point tuning distance in an aberration-free sample of 0.2-μm-diameter fluorescent beads in agarose (Supplementary Fig. 4a,b). The experimentally measured resolutions were used as benchmarks to evaluate the performance of the conjugate α-FSS–3PM in all in vitro and in vivo study. It should be noted that, for the imaging at depth >400 μm, the excitation beam is larger than SLM, resulting in reduced effective NA and resolution (Supplementary Fig. 4b).

As can be seen in Fig. 1f,g and Supplementary Fig. 3c,d, the effective FOV after a single correction of conjugate AO is extended to 150 μm and 400 μm in the lateral and axial directions, respectively, which corresponds to an increase of corrective volume by more than 100-fold compared to pupil AO configuration. Moreover, because axial scanning is achieved through remote focusing without requiring physical translation of the objective and wavefront corrector, fast axial scanning across different imaging planes can be easily achieved. Indeed, it should be noted that the enhancement of fluorescence intensity decreases when the imaging plane is away from the correction depth at 300 μm (Supplementary Fig. 3c,d). This may be due to the fact that the intact skull (100 μm thick) is not an infinitely thin layer of dominant aberration, and the corrective phase pattern measured at one location is not optimal for other locations.

We next validated the ability of conjugate α-FSS–3PM to improve in vivo brain imaging through the intact skull. We obtained in vivo images of microglia labeled with green fluorescent protein (GFP) in adult Cx3Cr1-GFP mice in either pupil or conjugate AO configuration. As shown in Supplementary Fig. 5, the detailed structures of microglia at 300 μm below the intact skull can barely be identified using a conventional 3P microscope (system AO correction). By using direct focus sensing with the GFP signal, pupil AO effectively compensates for the specimen-induced aberrations and successfully recovers the processes of microglia with fewer than three iterations (Supplementary Fig. 6), but its effective FOV is restricted to less than 30 μm (Supplementary Fig. 5a). By contrast, conjugate AO not only delivers similar improvements in resolution and signal intensity as those of pupil AO, enabling microglial processes to be clearly resolved, but also substantially enlarges the corrected FOV to 120 μm (Supplementary Fig. 5b,f). Furthermore, conjugate AO with remote focusing enables effective improvement of imaging resolution over large imaging depths ranged from 100 μm to 500 μm, with a single corrective wavefront at 300 μm (Supplementary Fig. 7 and Supplementary Video 1), similar to the in vitro experiment results (Fig. 1e–g). It was found that, despite the aberrations in deeper brain
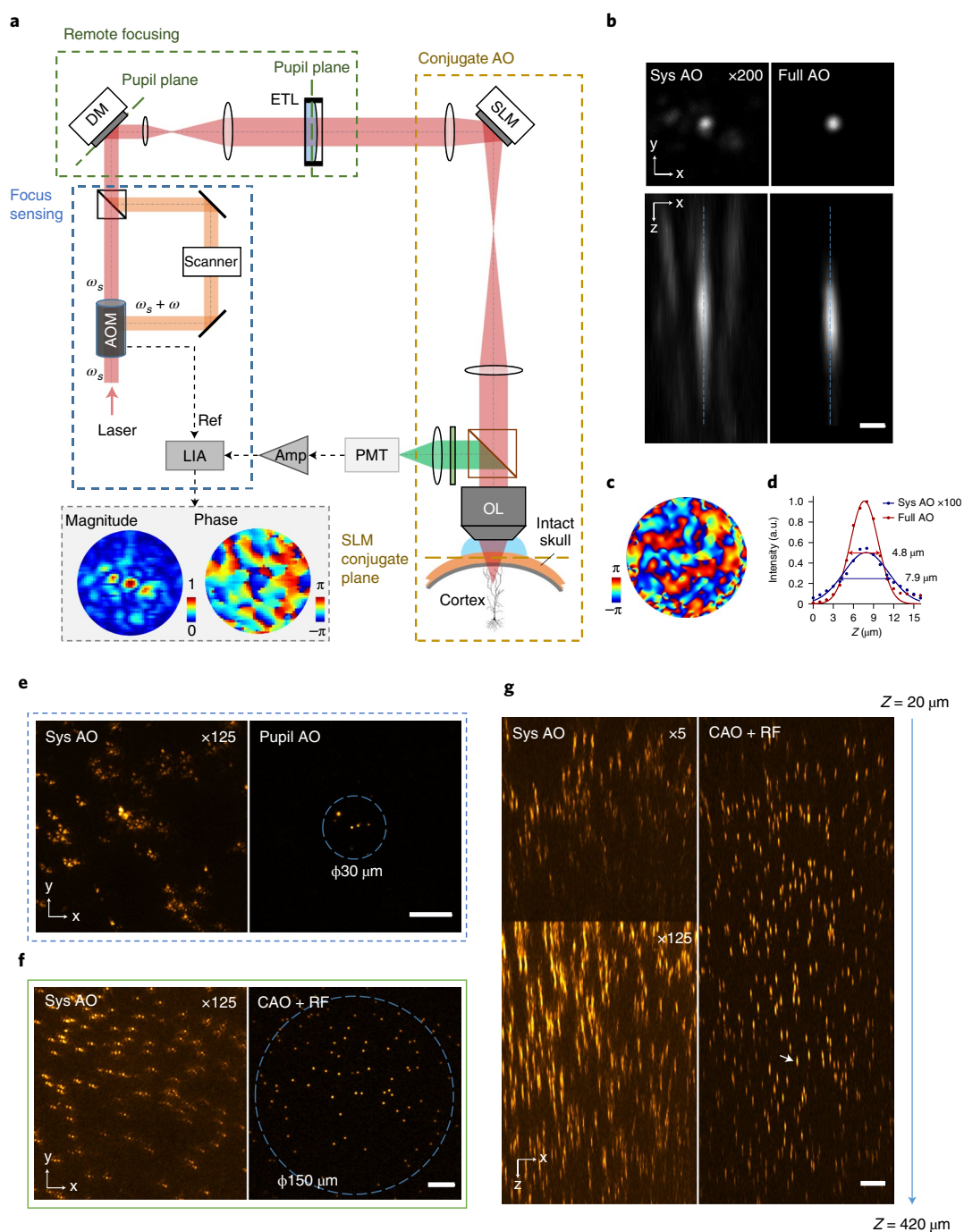
Fig. 1 | Conjugate α-FSS–3PM system and correction of aberrations induced by a 100-µm-thick intact mouse skull. a, Simplified schematic diagram of the conjugate α-FSS–3PM system. Blue dashed rectangle: focus sensing module; yellow dashed rectangle: conjugate AO (CAO) module; green dashed rectangle: RF module. See Supplementary Fig. 1 for the detailed optical path. **b,** X–Y and X–Z views of a fluorescent bead (1-µm diameter, 300 µm below skull) image with system correction only (left) and with full correction (right). The images with system correction have been enhanced 200-fold digitally as indicated for better visualization. Scale bar, 2 µm. **c,** Correction phase pattern applied to the SLM. **d,** Fluorescence signal profiles along the dashed lines in **b** are plotted with a curve fitted using a Gaussian function. Full width at half maximum (FWHM): 7.9 µm and 4.8 µm for system and full AO, respectively. **e,** X–Y view fluorescent beads (300 µm below skull) image with system correction only (left) and with full correction of pupil AO (right). Image of system AO was digitally enhanced as indicated for better visualization. Blue dashed circle indicates the effective FOV. Scale bar, 20 µm. **f,** X–Y view of fluorescent beads (300 µm below skull) image with system correction only (left) and with full CAO+RF correction (right). Blue dashed circle indicates the effective FOV. Scale bar, 20 µm. **g,** X–Z view with system correction only (left) and with full CAO+RF correction (right). White arrow indicates the fluorescent bead used for aberration measurement. Scale bar, 20 µm. a.u., arbitray units.

regions (for example, at 490 µm) that may require a corrective phase pattern covering a larger skull area, the corrective wavefront measured at 300 µm still shows an improved signal intensity (three-fold), as shown in Supplementary Fig. 8. This signal gain is essential for subsequent direct focus sensing at 490 µm due to the limited photon budget at depth. Therefore, we developed a pre-compensation

strategy to measure the E-field PSF in deeper regions of the brain (Methods). In brief, the additional corrective phase measured at current depth was added to that measured at the previous depth to generate the final and optimal phase pattern for full AO correction (Supplementary Fig. 8c). In this way, we can effectively measure the aberrations at depth and further enhance the signal intensity and spatial resolution (Supplementary Fig. 8a,b). These results reveal the great advantages of conjugate α-FSS AO with remote focusing for in vivo high-resolution imaging of mouse cortices through the intact skull over large volumes.

Structural and functional imaging of brain through intact skull. Next, we conducted in vivo imaging of neuronal and vascular structures in the mouse cerebral cortex through the intact skull. Figure 2a shows a cortical column of an adult Thy1-YFP transgenic mouse with a 100-μm-thick skull. Detailed experimental parameters are summarized in Supplementary Table 1. Here, dual-color fluorescence imaging of YFP-labeled pyramidal neurons and Texas Red-labeled cerebral microvasculature is achieved with single-wavelength (1,300 nm) 3P excitation[22]. As can be seen, even with system aberrations corrected, contrast and resolution in 3P imaging through the intact skull degrades rapidly with increase of depth (Fig. 2a and Supplementary Fig. 9), primarily because of the distortion of excitation PSF caused by skull-induced aberrations. The deterioration in PSF is particularly problematic in 3P imaging because the fluorescence has a third-order dependence on excitation density[3]. Thus, small neuronal dendrites, which have a very low level of fluorescence emission, can barely be visualized by conventional 3P imaging beyond 200-μm depth through the intact skull[23] (Supplementary Fig. 9). With the highly sensitive α-FSS method, both the aberrations and scattering experienced by the excitation light can be determined accurately and corrected effectively within 2–3 iterations. In this way, AO recovery of optimal PSF leads to much improved resolution with significantly stronger signals (up to 40-fold), allowing fine structures, such as neuronal dendrites and individual spines, to be visualized clearly through the intact skull (Fig. 2b–i and Supplementary Fig. 9). Note that the signal improvement in in vivo imaging is smaller than that of fluorescent beads at the same depth below the intact skull. This could be attributed to that (1) the size of dendrite is larger than the 1-μm-diameter beads; (2) the motion effect, such as heart beating and breathing, would inevitably cause error in the in vivo PSF measurement; and (3) the scattering of cortical tissue also lowers the signal increase to a certain extent. It is interesting that the correction phase patterns in Fig. 2d,h are smoother in the center region. It might be due to that the center rays that enter the specimen with lower incident angle have shorter light–tissue interaction lengths and, thus, experience less aberration and scattering than the marginal rays. Through-skull imaging of microvascular structures is also substantially improved after full AO correction, with much increased signal-to-background ratio (SBR) at depths (Supplementary Fig. 10). Quantitative measurement of the fluorescence intensity profiles of dendrites at depths provides an upper-bound estimation of the axial resolutions (Supplementary Fig. 11), indicating that conjugate α-FSS–3PM successfully restores

the synaptic resolution up to 550 μm and subcellular resolution up to 750 μm below pia. Note that the resolution after AO correction became poorer with increasing depth. This could be caused by the decrease of effective NA due to (1) loss of marginal rays from the scattering of brain volume and (2) beam clipping at the SLM using remote focusing when imaging deep region.

By virtue of the rapid direct focus sensing, we also applied the conjugate α-FSS–3PM to functional calcium imaging of neuronal activity, in which the fluorescence levels change rapidly and cannot be used for aberration measurement in most indirect AO approaches[24,25]. For direct focus sensing to work effectively, we normalized the outputs of lock-in detected signal (AC term) to the fluorescence signal (DC term) during focus sensing with fluctuating fluorescence (Methods). In this way, the artifact in the measured E-field PSF caused by rapidly varying calcium fluorescence can be eliminated, enabling the aberrations to be determined accurately (Supplementary Fig. 12). We next performed in vivo calcium imaging of GCaMP6s-labeled neurons in the somatosensory cortex of CCK-GCaMP6s transgenic mice through the intact skull. As shown in Fig. 3, with system AO alone, the calcium signals from the dendrite became undetectable because of the overwhelming background noise or so-called neuropil contaminations[26], which are especially problematic in the densely labeled brain. With α-FSS AO correction, the fluorescence signals from the neuronal soma and dendrites were increased significantly together with substantially improved resolution, enabling the recording of synchronized somato-dendritic activities (trace 1 and trace 2 in Fig. 3d,e). In addition, due to the large imaging volume and fast axial scanning provided by the conjugate AO with the remote focusing method, we demonstrated near-simultaneous multi-plane calcium imaging of neuronal and dendritic activities from different cortical layers through the intact skull (Supplementary Fig. 14 and Supplementary Video 2).

Microglia, which are the primary resident immune cells of the central nervous system, play essential roles in brain homeostasis and neurodegenerative diseases[27]. Non-invasive imaging tools with high-resolution capability are crucial for the study of undisturbed microglial physiology. Taking advantage of our conjugate α-FSS AO approach, we conducted in vivo through-skull imaging of microglia in the cerebral cortex of Cx3Cr1-GFP transgenic mice. As can be seen in Fig. 4a–c, conjugate AO consistently improved the image resolution and fluorescence signal, enabling us to resolve the fine processes of resting ramified microglia over large imaging volumes, which were otherwise not discernable without full AO correction. Moreover, by compensating for the specimen-induced aberrations and recovering a tight laser focus inside the cortex, α-FSS allows us to perform precise laser microsurgery through the intact skull, which is a powerful technique for studying the cellular mechanisms underlying various pathological conditions[28,29]. Time-lapse imaging at multiple depths revealed that the highly localized lesion activated only a few adjacent microglia (within a distance of 50 μm), which rapidly extended their processes toward the lesion in a coordinated manner (Fig. 4a and Supplementary Video 3). Here, it should be emphasized that we could not induce any laser ablation without AO correction under the same conditions. These results

Fig. 2 | Conjugate α-FSS–3PM enables in vivo cortical imaging with high resolution over large volumes through the intact skull. a, 3D reconstructions of in vivo dual-color 3P imaging of YFP-labeled neurons (orange) and Texas Red Dextran-labeled blood vessels (red) in a 150 × 150 × 780-μm³ cortical column of a 2-month-old Thy1-YFP transgenic mouse through 100-μm-thickness intact skull. Signal from skull (gray) is THG. The zero depth is set just beneath the pia. Three correction patterns were obtained and used to recover the imaging performance over the depth range of 0–360 μm, 360–540 μm and 540–800 μm, respectively (Supplementary Table 1). **b**, Maximum intensity projection (MIP) of stack images (545–555 μm below pia) of YFP-labeled pyramidal neurons from **a** with system correction only (left) and with full correction (right). The image of system AO correction was digitally enhanced as indicated for better visualization. Scale bar, 20 μm. **c**, Magnified views of dendrites in white box in **b**. White arrowheads indicate the dendritic spines. Scale bar, 5 μm. **d**, Correction phase pattern of SLM for the full AO image in **b**. **e**, Signal profiles along the dashed line in **c**. **f**, MIP of stack images (657–747 μm below pia) of pyramidal neurons from **a** with only system correction (left) and with full correction (right). Scale bar, 20 μm. **g**, Magnified views of neurons in white box in **f**. Scale bar, 10 μm. **h**, Correction phase pattern of SLM for the full AO image in **f**. **i**, Signal profiles along the dashed line in **g**. a.u., arbitray units.

revealed the great potential of α-FSS for precise optical manipulation, in addition to high-resolution imaging of brain through the intact skull.

Finally, we assessed the capability of our conjugate α-FSS AO for in vivo cortical imaging of aged (>10-month-old) mice with thicker skulls (130–140 μm) and mice with mechanically thinned skulls
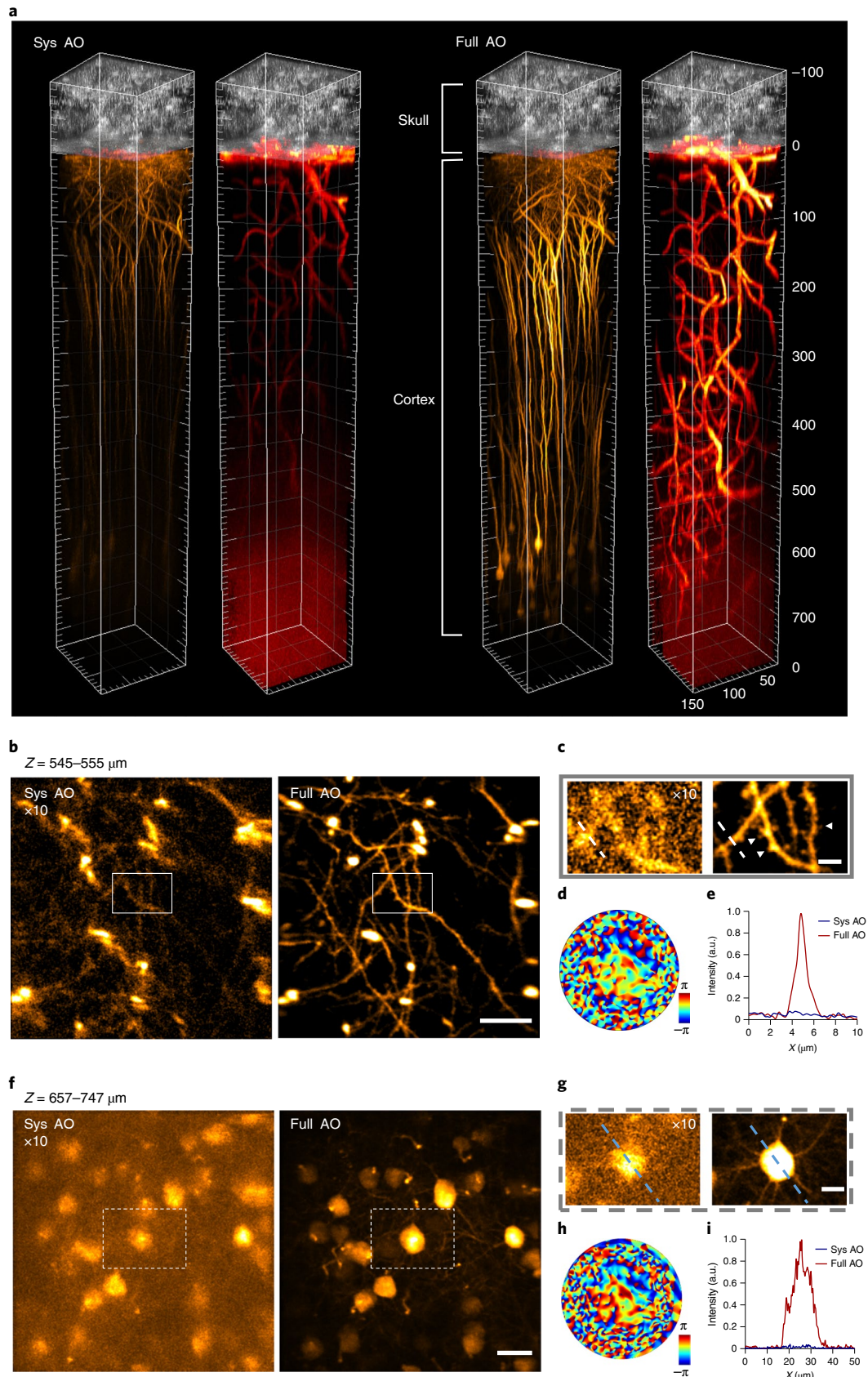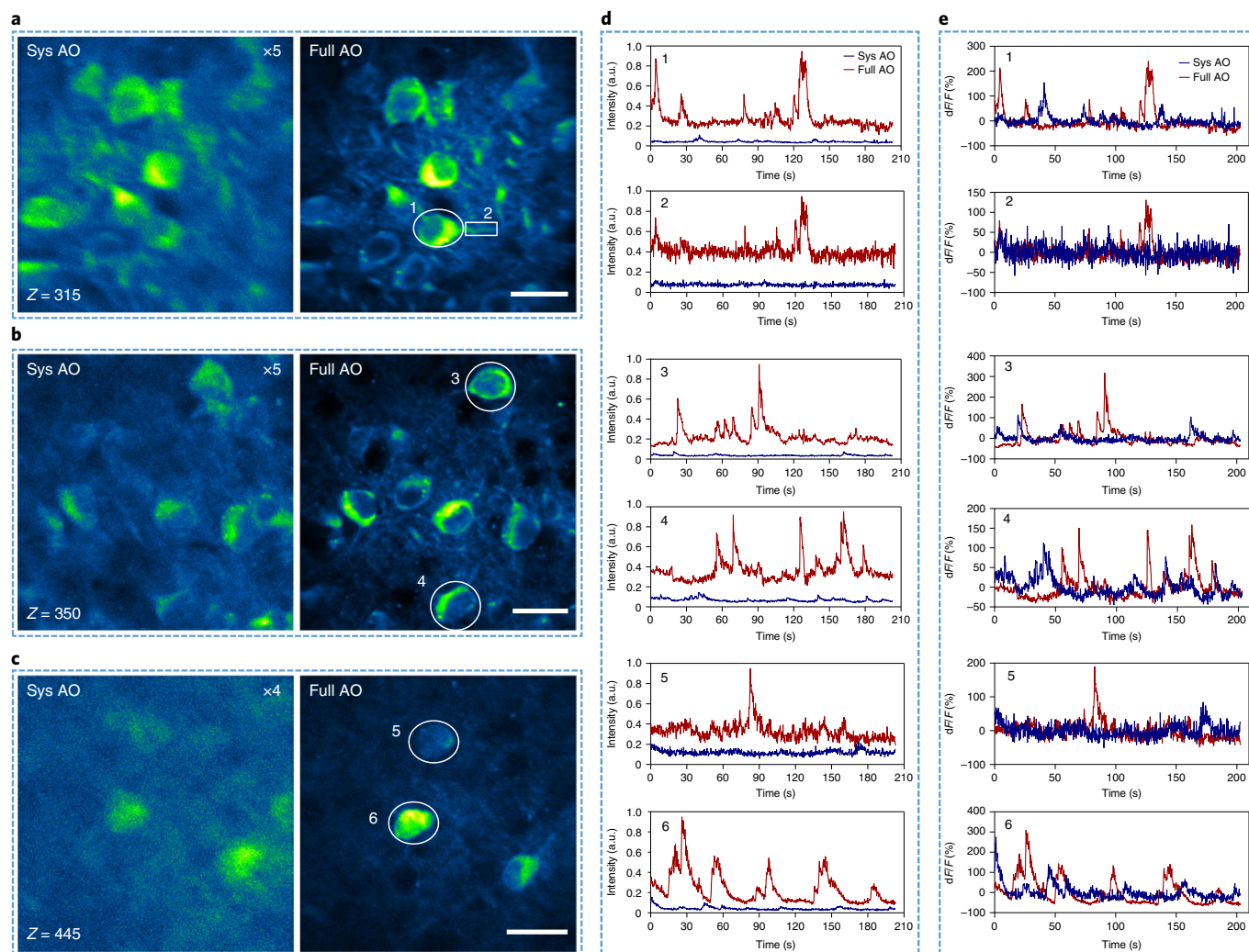
Fig. 3 | Conjugate α-FSS–3PM improves in vivo functional calcium imaging of neuronal activity through the intact skull. a–c, In vivo 3P calcium imaging of spontaneous neuronal activity at different depths below pia of the somatosensory cortex of a CCK-GCaMP6s mouse (4-month-old) through the intact skull (110-μm thickness) with system correction only (left) and full AO correction (right). Images are acquired at 4.43 frames per second and shown as average-intensity projections of 900 frames. Scale bar, 20 μm. **d**, Fluorescence traces extracted from the numbered ROIs as shown in **a–c**. **e**, Corresponding calcium-dependent fluorescence changes (d*F/F*). a.u., arbitrary units.

(~50 μm), respectively. The results presented in Supplementary Fig. 14–18 demonstrate that our AO-assisted through-skull imaging approach can facilitate in vivo studies of aged mouse brain and achieve better performance through the thinned skull than intact skull. In addition, we performed in vivo through-skull imaging of microglia in a mouse model of Alzheimer's disease (AD), in which amyloid plaques accumulate in the brain through aging and are thought to be the causative agent of AD pathology[30]. The morphology of microglia surrounding the amyloid plaques could be clearly resolved through a 140-μm-thick intact skull, which were otherwise unidentifiable without full AO correction (Fig. 4d). The observed morphology of the plaque-associated microglia is consistent with our previous study[31–33].

Imaging of deep brain through an open skull window. To push the imaging depth further, we performed 3P imaging through an open skull window, where a section of skull bone is replaced by a transparent glass to provide direct optical access to the brain[34,35]. In this case, the brain remains intact, and specimen-induced aberration mainly arises from the brain tissue, which accumulates with imaging depth, without contribution from any specific dominant

layer. Therefore, we reconfigured our AO 3P microscope system into the pupil conjugation with a high excitation NA of 1.05 to image the mouse brain at a higher resolution (Methods). We imaged the pyramidal neurons throughout the cerebral cortex in vivo, as shown in Fig. 5a. Here, α-FSS leads to significant increases in 3P signal (~9-fold) and recovery of synaptic resolution in the deepest cortical layer, allowing individual spines of basal dendrites to be clearly visualized (Fig. 5b–d and Supplementary Fig. 19).

Because of limits imposed by the thick and scattering cerebral cortex, it still remains a challenging task to achieve in vivo high-resolution imaging beyond the cortex and into the subcortical regions (for example, hippocampus) without using highly invasive procedures, such as GRIN lens insertion[36,37] and cortical tissue aspiration[38]. Previous work on 3P imaging of the hippocampus in vivo provided imaging resolution at the cellular level[3,4]. As shown in Fig. 5e, despite the neuronal somata in hippocampus CA1 being identifiable in conventional 3P imaging (system AO), the dendritic structures are still unresolvable due to brain-induced aberration (Fig. 5e,i). With pupil α-FSS AO, however, we substantially improved the 3P fluorescence signal and successfully restored synaptic resolution, allowing the apical dendritic spines
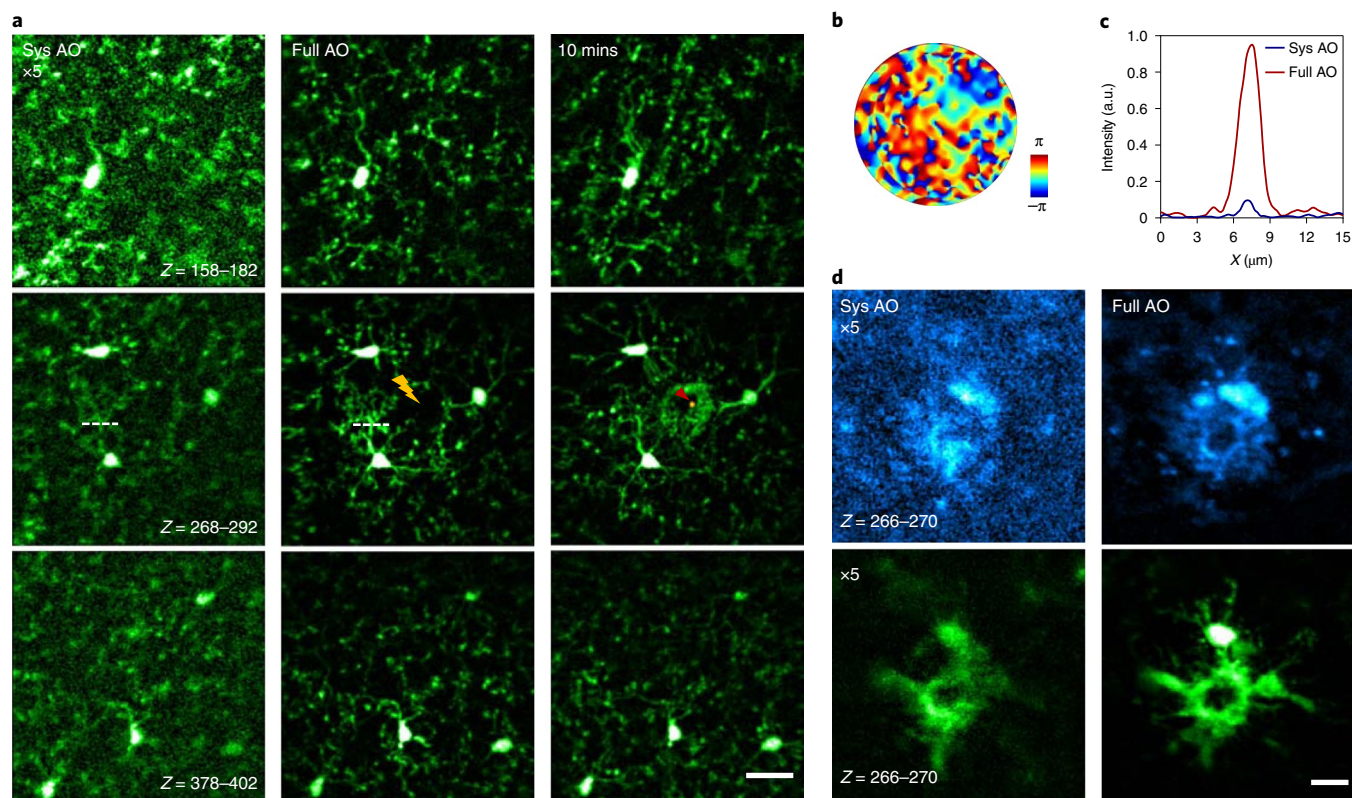
Fig. 4 | Conjugate α-FSS–3PM enables precise laser micro-lesion and in vivo high-resolution imaging of microglia in aged AD brain through the intact skull. a, Time-lapse images of GFP-labeled microglia in a Cx3Cr1-GFP transgenic mouse (2-month-old) after precise laser micro-lesion. Images are shown as maximum intensity projection acquired at different imaging depths with system correction only (left) and with full correction (middle and right). The images with system AO correction have been enhanced five-fold digitally for better visualization. The lightning symbols indicate the spot for subsequent laser ablation. The red arrow in the 10-minute image indicates the localized spot of micro-lesion. Scale bar, 20 μm. The detailed activation of microglia and laser lesion over 2 hours is illustrated in Supplementary Video 3. Here, the α-FSS was performed only once before laser ablation, and we found that the AO correction was valid over a long period (>2 hours) during following in vivo time-lapse imaging. **b**, Correction phase pattern of SLM for the full AO image in **a**. **c**, Signal profiles along the dashed line in **a**. **d**, Dual-color imaging of microglia expressing GFP (green channel) and amyloid plaque labeled by MeO-X04 (blue channel) in a 12-month-old APP/PS1×Cx3Cr1-GFP mouse through a 140-μm-thick intact skull. Scale bar, 10 μm. a.u., arbitray units.

of hippocampal CA1 neurons to be clearly resolved at depths up to 1,140 μm below pia (Fig. 5e–l and Supplementary Fig. 20).

Discussion

In this study, we developed an AO 3PM technique that incorporates two innovations: direct focus sensing with a phase-sensitive detection and conjugate AO with remote focusing. The phase-sensitive detection technology is crucial for the accurate determination of the scattered and aberrated focal field, thus allowing effective correction of both aberrations and scattering induced by the specimen. We conducted a series of experiments to make detailed comparison in the E-field measurement between the phase modulation with lock-in detection method used in α-FSS and the phase-stepping method used in previous studies[15,16]. We found that the signal-to-noise ratio (SNR) of the phase modulation with lock-in detection method was generally higher than the phase-stepping method (Supplementary Fig. 22), demonstrating superior performance of the phase-sensitive detection method in the suppression of noise, which enables accurate and rapid correction of sample-induced aberration. This is critical for in vivo imaging in deep tissue because of the limited photon budget and effect of motion artifact on PSF measurement. Here, it should be noted that the lock-in phase detection in α-FSS and the phase stepping in F-SHARP are fundamentally equivalent in terms of signal analysis, when phase stepping is performed over multiple cycles.

Unlike F-SHARP, α-FSS can push the frequency of phase-sensitive detection to the MHz range, which is advantageous due to 1/f laser noise (see details in Discussion of Supplementary Fig. 22).

The conjugate AO integrated with remote focusing ensures that a single corrective phase pattern can reliably recover high imaging resolution over a large imaging volume below a single turbid layer. Using the conjugate α-FSS–3PM system, we performed in vivo brain imaging through the intact skull, a desirable near-non-invasive but also considerably challenging approach. By correcting the specimen-induced aberrations, we achieved in vivo high-resolution imaging of mouse cortices up to 750 μm below the pia through the intact skull. With the great speed of direct focus sensing, we showed in vivo functional calcium imaging of densely labeled neurons at depth with substantially improved sensitivity and accuracy. By virtue of the tight focus recovered by AO, we also demonstrated precise laser microsurgery in mouse cortices through the intact skull and high-resolution dynamic imaging of the microglial responses. To push the depth limit further, we also performed in vivo imaging through the open skull window with pupil AO, which enables in vivo imaging of deep-cortical and subcortical structures at synaptic resolution up to 1.1 mm below pia within the intact brain. Our results demonstrate that the α-FSS technology holds great potential to advance in vivo imaging techniques and facilitate neuroscience study in living brain. It should be noted that direct focus sensing can also be achieved by either fluorescence or THG signals from blood
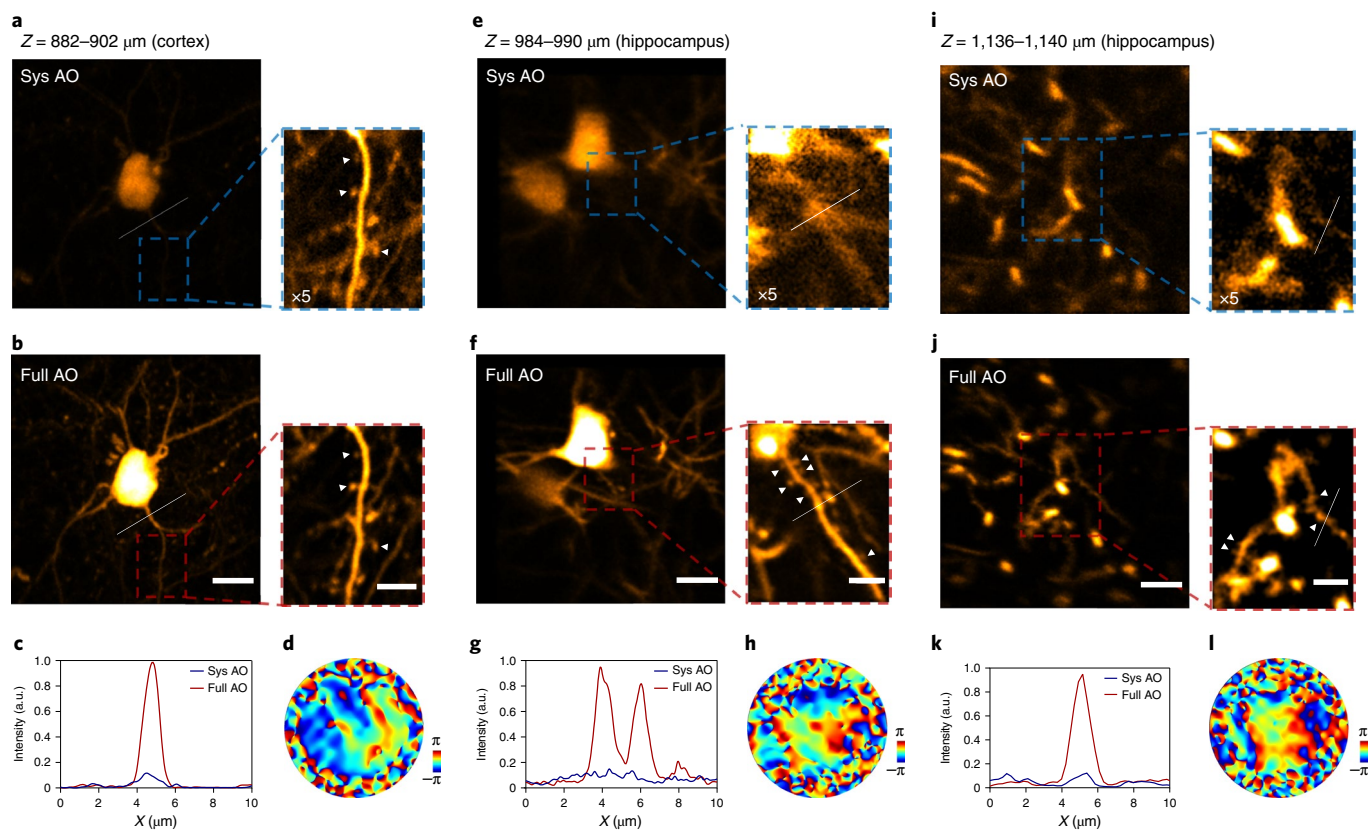
Fig. 5 | Pupil α-FSS–3PM enables in vivo imaging of deep-cortical and hippocampal neurons at synaptic resolution through an open skull window.
a,b, Maximum intensity projection (MIP) images of GFP-labeled cortical neurons ($Z = 882$–$902\,\mu m$ below pia) in a Thy1-GFP mouse (2-month-old) with system correction only (**a**) and with full correction (**b**). Scale bar, $10\,\mu m$. Insets display magnified views of neuronal dendrites from the outlined regions. White arrowheads indicate the dendritic spines. Scale bar, $5\,\mu m$. **c**, Signal profiles along the white line in **a**,**b**. **d**, Correction phase pattern of SLM in **b**. **e,f**, MIP images of hippocampal CA1 neuron ($Z = 984$–$990\,\mu m$ below pia) in a Thy1-GFP mouse with system correction only (**e**) and with full correction (**f**). Scale bar, $10\,\mu m$ and $5\,\mu m$ (insets). **g**, Signal profiles along the white line in insets of **e**,**f**. **h**, Correction phase pattern of SLM in **f**. **i,j**, MIP images of hippocampal CA1 neuron ($Z = 1,136$–$1,140\,\mu m$ below pia) with system correction only (**i**) and with full correction (**j**). Scale bar, $10\,\mu m$ and $5\,\mu m$ (insets). **k**, Signal profiles along the white line in insets of **i**,**j**. **l**, Correction phase pattern of SLM in **j**. a.u., arbitray units.

vessel, although the accuracy is slightly compromised by artifacts arising from the motion of red blood cells (Supplementary Fig. 21).

Although we have demonstrated the capability of α-FSS–3PM for deep brain imaging at 1,300-nm excitation, it can be applied to 1,700-nm excitation without any difficulty. Theoretically, for a larger imaging depth, 3P excitation at 1,700 nm is advantageous due to the longer effective attenuation length (~ 300 μm for 1,300 nm and ~ 400 μm for 1,700 nm in mouse gray matter)[3]. However, because the maximum excitation power should not exceed 100 mW to avoid tissue damage[39], the imaging depth is limited by the weak signal in deeper brain due to the inefficient 3P excitation. It has been reported that quantum dots have a 3P excitation cross-section of 4–5 orders of magnitude larger than those of conventional fluorescent dyes and have enabled 3P imaging of mouse cerebral vasculature at up to 2.1-mm depth[40]. As the 3P fluorescence signal from blood vessel can also be used for α-FSS, it may serve as a start point for full correction of aberrations in deeper brain region, which substantially boosts the fluorescence intensity of cellular structures labeled with fluorescent markers and allows for a second correction of residual aberrations based on the fluorescent proteins.

Online content

Any methods, additional references, Nature Research reporting summaries, source data, extended data, supplementary information, acknowledgements, peer review information; details of

author contributions and competing interests; and statements of data and code availability are available at https://doi.org/10.1038/s41587-022-01343-w.

References
1. Helmchen, F. & Denk, W. Deep tissue two-photon microscopy. *Nat. Methods* **2**, 932–940 (2005).
2. Theer, P. & Denk, W. T. On the fundamental imaging-depth limit in two-photon microscopy. *Proc. SPIE 5463, Femtosecond Laser Applications in Biology*. https://doi.org/10.1117/12.548057 (2004).
3. Horton, N. G. et al. In vivo three-photon microscopy of subcortical structures within an intact mouse brain. *Nat. Photonics* **7**, 205–209 (2013).
4. Ouzounov, D. G. et al. In vivo three-photon imaging of activity of GCaMP6-labeled neurons deep in intact mouse brain. *Nat. Methods* **14**, 388–390 (2017).
5. Kubby, J. A. *Adaptive Optics for Biological Imaging* (CRC Press, 2013).
6. Booth, M. J. Adaptive optical microscopy: the ongoing quest for a perfect image. *Light Sci. Appl.* **3**, e165 (2014).
7. Ji, N. Adaptive optical fluorescence microscopy. *Nat. Methods* **14**, 374–380 (2017).
8. Wang, K. et al. Rapid adaptive optical recovery of optimal resolution over large volumes. *Nat. Methods* **11**, 625–628 (2014).
9. Wang, K. et al. Direct wavefront sensing for high-resolution in vivo imaging in scattering tissue. *Nat. Commun.* **6**, 7276 (2015).

10. Liu, R., Li, Z., Marvin, J. S. & Kleinfeld, D. Direct wavefront sensing enables functional imaging of infragranular axons and spines. *Nat. Methods* **16**, 615–618 (2019).
11. Débarre, D. et al. Image-based adaptive optics for two-photon microscopy. *Opt. Lett.* **34**, 2495 (2009).
12. Ji, N., Milkie, D. E. & Betzig, E. Adaptive optics via pupil segmentation for high-resolution imaging in biological tissues. *Nat. Methods* **7**, 141–147 (2010).
13. Tang, J., Germain, R. N. & Cui, M. Superpenetration optical microscopy by iterative multiphoton adaptive compensation technique. *Proc. Natl Acad. Sci. USA* **109**, 8434–8439 (2012).
14. Wang, C. et al. Multiplexed aberration measurement for deep tissue imaging in vivo. *Nat. Methods* **11**, 1037–1040 (2014).
15. Papadopoulos, I. N., Jouhanneau, J.-S., Poulet, J. F. A. & Judkewitz, B. Scattering compensation by focus scanning holographic aberration probing (F-SHARP). *Nat. Photonics* **11**, 116–123 (2017).
16. Papadopoulos, I. N. et al. Dynamic conjugate F-SHARP microscopy. *Light Sci. Appl.* **9**, 110 (2020).
17. Yaqoob, Z., Psaltis, D., Feld, M. S. & Yang, C. Optical phase conjugation for turbidity suppression in biological samples. *Nat. Photonics* **2**, 110–115 (2008).
18. Xu, H.-T., Pan, F., Yang, G. & Gan, W.-B. Choice of cranial window type for in vivo imaging affects dendritic spine turnover in the cortex. *Nat. Neurosci.* **10**, 549–551 (2007).
19. Nimmerjahn, A. Optical window preparation for two-photon imaging of microglia in mice. *Cold Spring Harb. Protoc.* **2012**, pdb.prot069286 (2012).
20. Park, J.-H., Sun, W. & Cui, M. High-resolution in vivo imaging of mouse brain through the intact skull. *Proc. Natl Acad. Sci. USA* **112**, 9236–9241 (2015).
21. Tao, X. et al. Three-dimensional focusing through scattering media using conjugate adaptive optics with remote focusing (CAORF). *Opt. Express* **25**, 10368–10383 (2017).
22. Hontani, Y., Xia, F. & Xu, C. Multicolor three-photon fluorescence imaging with single-wavelength excitation deep in mouse brain. *Sci. Adv.* **7**, eabf3531 (2021).
23. Wang, T. et al. Three-photon imaging of mouse brain structure and function through the intact skull. *Nat. Methods* **15**, 789–792 (2018).
24. Streich, L. et al. High-resolution structural and functional deep brain imaging using adaptive optics three-photon microscopy. *Nat. Methods* **18**, 1253–1258 (2021).
25. Rodríguez, C. et al. An adaptive optics module for deep tissue multiphoton imaging in vivo. *Nat. Methods* **18**, 1259–1264 (2021).
26. Göbel, W. & Helmchen, F. In vivo calcium imaging of neural network function. *Physiology Bethesda* **22**, 358–365 (2007).
27. Parkhurst, C. N. & Gan, W.-B. Microglia dynamics and function in the CNS. *Curr. Opin. Neurobiol.* **20**, 595–600 (2010).
28. Canty, A. J. et al. In-vivo single neuron axotomy triggers axon regeneration to restore synaptic density in specific cortical circuits. *Nat. Commun.* **4**, 2038 (2013).
29. Nishimura, N. et al. Targeted insult to subsurface cortical blood vessels using ultrashort laser pulses: three models of stroke. *Nat. Methods* **3**, 99–108 (2006).
30. Karran, E., Mercken, M. & De Strooper, B. The amyloid cascade hypothesis for Alzheimer's disease: an appraisal for the development of therapeutics. *Nat. Rev. Drug Discov.* **10**, 698–712 (2011).
31. Lau, S.-F. et al. IL-33-PU.1 transcriptome reprogramming drives functional state transition and clearance activity of microglia in Alzheimer's disease. *Cell Rep.* **31**, 107530 (2020).
32. Chen, C. et al. High-resolution two-photon transcranial imaging of brain using direct wavefront sensing. *Photonics Res.* **9**, 1144–1156 (2021).
33. Chen, C. et al. In vivo near-infrared two-photon imaging of amyloid plaques in deep brain of Alzheimer's disease mouse model. *ACS Chem. Neurosci.* **9**, 3128–3136 (2018).
34. Holtmaat, A. et al. Long-term, high-resolution imaging in the mouse neocortex through a chronic cranial window. *Nat. Protoc.* **4**, 1128–1144 (2009).
35. Kim, T. H. et al. Long-term optical access to an estimated one million neurons in the live mouse cortex. *Cell Rep.* **17**, 3385–3394 (2016).
36. Barretto, R. P. J., Messerschmidt, B. & Schnitzer, M. J. In vivo fluorescence imaging with high-resolution microlenses. *Nat. Methods* **6**, 511–512 (2009).
37. Qin, Z. et al. Adaptive optics two-photon endomicroscopy enables deep-brain imaging at synaptic resolution over large volumes. *Sci. Adv.* **6**, eabc6521 (2020).
38. Dombeck, D. A., Harvey, C. D., Tian, L., Looger, L. L. & Tank, D. W. Functional imaging of hippocampal place cells at cellular resolution during virtual navigation. *Nat. Neurosci.* **13**, 1433–1440 (2010).
39. Wang, T. & Xu, C. Three-photon neuronal imaging in deep mouse brain. *Optica* **7**, 947–960 (2020).
40. Liu, H. et al. In vivo deep-brain structural and hemodynamic multiphoton microscopy enabled by quantum dots. *Nano Lett.* **19**, 5260–5265 (2019).

Methods

Conjugate α-FSS–3PM system. A detailed schematic diagram of our 3P microscope system is shown in Supplementary Fig. 1. The excitation was a laser of 1,300 nm and 1-MHz repetition rate. A homebuilt single-prism pulse compressor was used to compensate for the group delay dispersion of the microscope system and laser source, yielding a final pulse duration of 60 fs reaching the sample[41]. The excitation laser then passed through an acousto-optic modulator (AOM). The 0th and 1st order diffracted beams were used as the stationary and scanning beams, respectively. The scanning beam was expanded to match the aperture of an X–Y galvanometric scanning mirror. An optical delay line (not shown in Supplementary Fig. 1) was placed in the scanning beam arm to match the path length of the two interferometer arms. The two beams were then combined by a polarizing beamsplitter and expanded to slightly overfill the aperture of the DM, which was used to correct for system aberrations based on a simple sensorless method[42]. A half-wave plate and a polarizer were placed before the DM to ensure the same polarization and also to adjust the intensity ratio of these two beams. The DM was conjugated to the 3-mm X-galvanometric scanning mirror via a 4f system. The X and Y scanning mirrors were mutually conjugated by lens pair L9 and L10, each of which consisted of two doublets in Ploessl configuration. Then, the galvanometric Y-scanning mirror was conjugated to an ETL by scan lens L11 and tube lens L12. The ETL was conjugated to the back aperture of a high-NA objective by a pair of achromatic doublets L13 and L14. A phase-only SLM was placed at ~85 mm after L13 and conjugated to the sample plane by the 4f system, consisting of L14 and the objective lens. The beam diameter entering the objective back aperture is ~11 mm, resulting an excitation NA of ~0.7. The objective was mounted on a motorized actuator for translation along the optical axis. The excited optical signal was collected by the same objective and directed to the photo-detection unit via dichroic mirror D1. An appropriate band-pass filter along with a short-pass filter were placed before the photomultiplier tube (PMT) module to detect the THG/ MeOX4, GFP/YFP/GCaMP6s or Texas Red signal. The current signal from the PMT was converted to voltage by a transimpedance current amplifier.

For 3P imaging, only the stationary beam was selected, and the scanning beam was blocked. The AOM was used to control the excitation power by adjusting the driving remote focusing (RF) power. Galvanometric scanning mirrors GM2x and GM2y were used for lateral scanning. The excited fluorescence signal was digitized at a sample rate of 120 MHz by a high-speed data acquisition card. The microscope control software was custom modified based on ScanImage 5.7 (ref. [43]). We synchronized the image acquisition to the laser clock such that each voxel was illuminated by a single or constant number of excitation pulses. In addition, we only sampled the fluorescence signal over a short time window (~50 ns) for each excitation pulse, whereas other samples where no signal was presented were rejected to improve the SNR.

Phase modulation and lock-in detection. α-FSS requires a linear phase modulation, equivalent to a frequency shift, of either scanning or stationary beam for lock-in detection (see 'Principle of α-FSS'). An AOM can be used as an optical frequency shifter to generate an accurate linear phase modulation to the weaker scanning beam. However, the AOM efficiency is low for a small frequency shift (for example, <1 MHz, the repetition rate of excitation laser). Because the excitation source is a periodic ultra-fast laser, we take advantage of this property and achieve low-frequency phase modulation with a single AOM. As shown in Supplementary Fig. 1, after being diffracted by the AOM, the wave function of the scanning beam can be written as

$$E_{scan}(t) = E_0 e^{j[2\pi[f_i + (Nf_r + f)]t]} \cdot \sum_{k=-\infty}^{+\infty} \delta\left(t - \frac{k}{f_r}\right)$$

$$= E_0 e^{j[2\pi(f_i+f)t]} \cdot \sum_{k=-\infty}^{+\infty} \delta\left(t - \frac{k}{f_r}\right) \cdot e^{j[2\pi(Nf_r)t]}$$

$$= E_0 e^{j[2\pi(f_i+f)t]} \cdot \sum_{k=-\infty}^{+\infty} \delta\left(t - \frac{k}{f_r}\right)$$

where f_i is the center frequency of excitation laser, f_r is the laser repetition rate and $(Nf_r + f)$ is the AOM driving frequency in which N is an integer and $|f| < f_r/2$. Here, the laser pulse is approximated with a δ-function, because the pulse duration (~60 fs) is much shorter than the period of laser cycle (~1 μs). Therefore, the frequency shift of $(Nf_r + f)$ is equivalent to a linear phase modulation at frequency f for a periodic ultra-fast laser. This effect is similar to the aliasing phenomenon in signal processing when a sinusoid is sampled at a frequency lower than the Nyquist frequency[44]. In our α-FSS-3PM, we chose $f_r = 1.002$ MHz, $f = 0.4$ MHz and $N = 65$, resulting in a driving frequency of $Nf_r + f = 65.5$ MHz for the AOM.

For signal demodulation, the 3P fluorescence excited by the interference of the stationary and scanning beams was first filtered by a low-pass and band-pass filter and then fed into a lock-in amplifier. To obtain the reference signal for the lock-in amplifier, the pulse train signal from the oscillator of the carbide pump laser (~65.1 MHz), which is the 65th harmonic frequency of the 3P excitation laser, was filtered using a band-pass filter and then frequency mixed with the AOM driving signal (65.5 MHz) using a custom-made RF mixer. The output signal from

the mixer was filtered by a low-pass filter and then used as the reference signal (0.4 MHz) for the lock-in amplifier. Both the in-phase and quadrature output of the lock-in amplifier were digitized by the data acquisition device and further processed in the control computer.

Focus sensing and shaping. To measure the PSF, both stationary and scanning beams were focused on the sample. The power of AOM driving signal and the angle of the half-wave plate were adjusted such that the intensity ratio of these two beams is ~10:1. Galvanometric scanner GM2x and GM2y were programmed to park the stationary beam at the target position, and scanner GM1 was selected to raster scan the weak probe beam against the strong image beam in a small region (10~20 μm). The total laser power was reduced to 70% of the imaging power (Supplementary Table 1) during focus sensing to avoid possible photo-bleaching or damage. The in-phase (X) and quadrature (Y) outputs of the lock-in amplifier were recorded, forming the real and imaginary parts of the measured E-field PSF (that is, $E = X + iY$; see 'Principle of α-FSS'). Also, the corrective phase pattern was the conjugate phase of the Fourier transform of the E-field PSF. Because the number of pixels of the PSF was much smaller than that of the SLM, zero padding was used before performing the Fourier transform.

To perform optical phase conjugation, the alignment of the SLM and back aperture of the objective needs to be calibrated. The detailed procedure was reported previously[15]. In brief, a known phase pattern was first displayed on the SLM, and the resulting aberrated PSF was measured using the method described above. The phase of the Fourier transform of the PSF represented the wavefront at the back aperture of the objective lens. Then, the affine transformation (rotation, scale and translation) between this wavefront and the phase pattern on the SLM was calibrated. With this information, we could add the affine transformation of the measured wavefront to the SLM and cancel out the aberrations. In the conjugate α-FSS–3PM system, because the SLM was not placed on the pupil conjugate plane, the diameter and position of laser beam on the SLM would change with the axial and lateral shift of the laser focus. To perform α-FSS at any desired position, we conducted a series of calibrations at different focal positions and stored the mapping in a lookup table to be loaded accordingly during in vivo imaging. The details are summarized in Supplementary Fig. 23.

Conjugate plane calibration. To achieve the optimal FOV for transcranial brain imaging, the SLM was required to be conjugated to the skull plane. The conjugate plane position of the SLM was calibrated by using a fluorescent target (a thin layer of dry rhodamine on a cover glass). First, the ETL was set to 0 diopter position, and the fluorescent target was placed at the natural focal plane of the objective using 3P fluorescence as guidance. We recorded the objective position as z_1. Next, a camera was placed before L12 to form a clear image of the SLM via lens L12 and L13. Finally, we translated the objective axially toward the sample using a motorized actuator until the fluorescent target could also be clearly resolved on the camera (that is, both the fluorescent target and the SLM were imaged on the same plane). The objective position at this step was z_2. The distance between the SLM conjugate plane and objective natural focal plane could be calculated as $\Delta z = z_2 - z_1$, which is ~350 μm in our setup. As shown in Supplementary Fig. 1, the SLM is conjugated to the dominant aberration layer (skull) via the 4f system consisting of the lens L14 and objective lens. As long as the distances between the SLM, lens L14 and the objective lens are fixed, the position of SLM conjugate plane is determined. It will remain unchanged regardless of the remote focusing at any imaging depths. Therefore, this calibration needs to be performed only once and remained unchanged for the rest of experiments. With this information, we can easily conjugate the SLM to the most aberrated plane in the biological sample. For example, to conjugate the SLM to a mouse skull, we adjust the position of the mouse head to ensure its skull to be at the position of SLM conjugate plane, instead of changing the position of SLM. In brief, we first set ETL to 0 diopter and then located the middle plane of the skull using the intrinsic THG signal. Next, we translated the objective 350 μm toward the sample, which ensured the conjugation of SLM and skull. After that, the position of objective and imaging sample remained unchanged such that the SLM could be always conjugated to the skull. For axial sectioning, the remote focusing module using the ETL was employed.

AO-corrected remote focusing. The ETL was used to scan the microscope focus axially by controlling the divergence of the excitation light entering the objective. The relationship of the focus shift and ETL control voltage was calibrated using 1-μm-diameter fluorescent beads. To achieve aberration-free remote focusing, a DM was placed on the pupil conjugate plane to compensate for the system aberrations at different focal planes. The aberrations were measured and corrected using a Zernike modal-based sensorless AO algorithm[42]. In brief, the 3P fluorescence intensity of a fluorescent solution (rhodamine 6G) was chosen as the optimization metric. Nine to eleven different values of each Zernike mode were sequentially applied to the DM, and the corresponding fluorescence intensity was Gaussian fitted to find the maximal point. This procedure was repeated for the first 36 Zernike modes (tip, tilt and defocus excluded). To achieve aberration-free imaging over a large depth range, we calibrated the system AO correction phase pattern over an axial range of $\Delta z = -300$ to 450 μm at an interval of 50 μm. We then fit the two coefficients for each Zernike mode measured 50 μm apart with a linear

function and interpolated the corresponding coefficient value for other focal shift[45]. The calibrations for the system aberrations at different focal planes were stored in a lookup table to be used as system AO correction for the conjugate AO imaging over large-volume or multi-plane imaging. The imaging performance of system AO correction was characterized using 0.2-μm-diameter fluorescent beads, as shown in Supplementary Fig. 4.

Pre-compensation strategy for conjugate α-FSS at depths. To perform AO correction at deep region, we first applied α-FSS at a shallower layer, where the signal quality is good enough for PSF sensing, and then used this correction pattern to partially compensate for the large aberrations at the deeper region, as shown in Supplementary Fig. 8. In this way, the fluorescence intensity in the deeper layer was greatly boosted, which enabled in situ PSF measurement. The residual wavefront aberration was calculated using the same method described in 'Focus sensing and shaping' and then added to the SLM to correct all the aberrations.

α-FSS using calcium indicator. Because the fluorescence of the calcium indicator fluctuates, α-FSS cannot be directly applied to calcium imaging. To solve this problem, we normalized the outputs of lock-in amplifier (AC term of the 3P signal excited by the interference of scanning and stationary beams) to the fluorescence signal intensity (DC term) during focus sensing (Supplementary Fig. 12). In brief, the amplified signal from the PMT was sampled by the data acquisition device and low-pass filtered at 10 Hz to extract the fluorescence fluctuation induced by calcium transients. Next, the outputs from the lock-in amplifier were normalized to this value at each scanning coordinate—that is, $E^n(x) = \frac{X(x)+iY(x)}{I(x)}$, where $X(x)$ and $Y(x)$ were the in-phase and quadrature outputs of the lock-in amplifier, and $I(x)$ was the low-pass-filtered fluorescence intensity.

Pupil α-FSS-3PM system. The SLM was moved from the sample conjugate plane to the pupil conjugate plane and replaced the original DM. The ETL was removed, and the actuator carrying the objective was employed for axial sectioning. Lens L5–L8 and L13 were changed accordingly to match the apertures of the SLM, scanning mirrors and objective (L5: f = 75, #45–805; L6: f = 150 mm, #47–380; L7: f = 200 mm, #47–271; L8: f = 75 mm, #45–805; L13: f = 150 mm, #47–380; Edmund Optics). The final beam diameter is ~15 mm at the objective back aperture, resulting in an excitation NA of 1.05.

System aberration correction. The system aberration for the pupil α-FSS-3PM system was measured and corrected using α-FSS. In brief, a flat pattern was projected on the SLM, and fluorescent beads were used as the imaging target. We parked the strong beam on a fluorescent bead and scanned the weak beam to measure the E-field PSF. Then, the phase of the Fourier transform of the PSF was applied to the SLM to correct the system aberration.

Animal preparation. All the animal experiments were conducted on adult mice (>2 months old). Five transgenic mouse lines—Thy1-YFP (Tg(Thy1-YFP)HJrs/J)[46], Thy1-GFP-M, Cx3Cr1-GFP (B6.129P2(Cg)-Cx3cr1tm1Litt/J)[47], CCK-GCaMP6s and APP-PS1/Cx3Cr1-GFP—were used. APP-PS1/Cx3Cr1-GFP mice were obtained by crossing APP-PS1 (Tg(APPswe,PSEN1dE9)85Dbo) mice with Cx3Cr1-GFP mice. CCK-GCaMP6s mice were generated by crossing CCK-ires-Cre (Ccktm1.1(cre)Zjh/J) mice with GCaMP6s-Dio (Ai162(TIT2L-GC6s-ICL-tTA2)-D) mice. All animal procedures were conducted in accordance with the Guidelines of the Animal Care Facility of the Hong Kong University of Science and Technology (HKUST) and were approved by the Animal Ethics Committee at HKUST.

Intact skull preparation. Before surgery, mice were anesthetized by intraperitoneal (i.p.) injection of ketamine–xylazine mixture. A midline scalp incision was performed to expose the skull, and the connective tissue attached to the skull was gently removed. Then, a custom-designed head plate with a circular center hole was glued to the exposed skull for head fixation during in vivo imaging. Dental cement was then applied to fill the gap between the head plate and skull and allowed to dry and harden. Finally, the exposed skull was protected by a biocompatible sealant (Kwik-Cast, World Precision Instruments), which can be peeled off before the imaging experiment.

Thinned skull window. The skull thinning procedure is slightly modified from a previous protocol[48]. In brief, a 0.5-mm carbon steel burr attached to a high-speed drill was used to thin a small circular region (diameter, 2.0–2.5 mm) centered at 3 mm posterior and lateral to the bregma point. After most of the middle spongy bone was removed, a microsurgical blade (no. 6961, Surgistar) was used to thin the skull manually to ~50-μm thickness, which can be accurately measured using the THG signal of skull bone.

Open skull window. Two types of open skull window were used in this study. For the imaging of deep cortex, the cranial window was prepared following a previous protocol[34]. For the imaging of hippocampus, a whole-brain glass window was implanted according to a previously published approach[35].

In vivo imaging. For morphological imaging, the mouse was anesthetized by an i.p. injection of ketamine–xylazine mixture or by inhalation of isoflurane (1–2% in oxygen). For the imaging of vasculature, mice received a retro-orbital intravenous injection of Texas Red (5 mg of dextran conjugate dissolved in 100 μl of sterile saline, 70-kDa molecular weight; Thermo Fisher Scientific). For imaging amyloid plaques, the APP-PS1/Cx3Cr1-GFP mice were i.p. injected with MeO-X04 (5.0 mg kg^{-1}, 10% DMSO and 90% PBS) 2 hours before imaging. For functional calcium imaging, the mice were under light anesthesia (<0.5% isoflurane) with their body confined in a tube to reduce motion. During in vivo imaging experiments, the mice were mounted on a head-holding stage with angle adjusters (NARISHIGE, MAG-2), and the mouse skull was aligned to be perpendicular to the objective axis by using THG signal of skull as guidance. The detailed imaging parameters, including excitation power, pixel dwell time, α-FSS measurement time and number of iterations, are summarized in Supplementary Table 1. It should be noted that the total time for α-FSS is dominated by the E-field PSF measurement (Supplementary Table 1). Additional time for Fourier transform calculation using a standard computer is short (<0.1 s) and negligible.

Multi-plane calcium imaging. We first measured and corrected the sample-induced aberrations using α-FSS and recovered optimal imaging performance over a large volume. We then picked three regions of interest (ROIs) and sequentially scanned the three ROIs at a frame rate of 10.7 Hz using ETL, resulting a volume rate of 3.6 Hz. The DM was synchronized with the ETL to compensate for the divergence-induced system aberrations, which were calibrated before the imaging experiment and stored in a lookup table.

AO-assisted laser microsurgery. To conduct laser-mediated microsurgery, the aberration induced by the biological sample was first corrected using α-FSS. Then, the 3P excitation laser was increased to ~110 mW post-objective and focused on the target point for ~10 s. The injured region was clearly indicated by the new fluorescence signal produced by the laser ablation process[49].

Image analysis. The images were processed with MATLAB or ImageJ[50]. To remove the inter-frame motion artifacts, images were registered using the TurboReg or StackReg plugin[51] in ImageJ. Some images were processed with the Smooth function in ImageJ, which replaced the value of each pixel with its 3×3 neighboring pixels, or with the Gaussian Blur function with sigma of 0.15–0.2 μm. The image pairs with system and full AO were acquired and processed using the same parameters. For the 'system AO' images where the signal intensity was too weak, a linear digital enhancement as indicated in the figures was applied for better visualization.

Statistics and reproducibility. For the in vitro experiments (Fig. 1b,e–g and Supplementary Figs. 3, 4 and 12), similar results were obtained on more than five measurements. For the in vivo experiments (Figs. 2–5 and Supplementary Figs. 5–11 and 13–21), similar measurements were performed on more than three mice.

Reporting summary. Further information on research design is available in the Nature Research Reporting Summary linked to this article.

Data availability

The authors declare that the main data supporting the findings of this study are available within the paper, its extended data and Supplementary Information files. The source data files for all data presented within the figures can be found at https://github.com/QuLabHKUST/QuLabAO.

Code availability

The custom codes for image processing are available online at https://github.com/QuLabHKUST/QuLabAO.

References

41. Akturk, S., Gu, X., Kimmel, M. & Trebino, R. Extremely simple single-prism ultrashort-pulse compressor. *Opt. Express* **14**, 10101–10108 (2006).
42. Park, J.-H., Kong, L., Zhou, Y. & Cui, M. Large-field-of-view imaging by multi-pupil adaptive optics. *Nat. Methods* **14**, 581–583 (2017).
43. Pologruto, T. A., Sabatini, B. L. & Svoboda, K. ScanImage: flexible software for operating laser scanning microscopes. *Biomed. Eng. Online* **2**, 13 (2003).
44. Oppenheim, A. V., Willsky, A. S. & Nawab, S. H. *Signals & Systems* (Prentice-Hall International, 1997).
45. Yang, Y., Chen, W., Fan, J. L. & Ji, N. Adaptive optics enables aberration-free single-objective remote focusing for two-photon fluorescence microscopy. *Biomed. Opt. Express* **12**, 354–366 (2021).
46. Feng, G. et al. Imaging neuronal subsets in transgenic mice expressing multiple spectral variants of GFP. *Neuron* **28**, 41–51 (2000).
47. Jung, S. et al. Analysis of fractalkine receptor CX₃CR1 function by targeted deletion and green fluorescent protein reporter gene insertion. *Mol. Cell. Biol.* **20**, 4106–4114 (2000).

48. Yang, G., Pan, F., Parkhurst, C. N., Grutzendler, J. & Gan, W.-B. Thinned-skull cranial window technique for long-term imaging of the cortex in live mice. *Nat. Protoc.* **5**, 201–208 (2010).
49. Sun, Q. et al. In vivo imaging-guided microsurgery based on femtosecond laser produced new fluorescent compounds in biological tissues. *Biomed. Opt. Express* **9**, 581–590 (2018).
50. Schindelin, J. et al. Fiji: an open-source platform for biological-image analysis. *Nat. Methods* **9**, 676–682 (2012).
51. Thévenaz, P., Ruttimann, U. E. & Unser, M. A pyramid approach to subpixel registration based on intensity. *IEEE Trans. Image Process.* **7**, 27–41 (1998).

Author contributions

Z.Q. and J.Y.Q. conceived of the research idea. Z.Q. built the AO 3P imaging system and created the control software. Z.Q., Z.S. and C.C. designed and conducted the experiments and data analysis. Z.S. carried out the surgery, with the assistance of C.C., Z.Q., W.W. and J.L. N.Y.I. and J.Y.Q. supervised the project. C.C. and Z.Q. took the lead in writing the manuscript, with input from all other authors.

Competing interests

Z.Q. and J.Y.Q. have submitted a patent application on part of the described work. The remaining authors declare no competing interests.

Additional information

Supplementary information The online version contains supplementary material available at https://doi.org/10.1038/s41587-022-01343-w.

Correspondence and requests for materials should be addressed to Jianan Y. Qu.

Peer review information *Nature Biotechnology* thanks Xi Chen and the other, anonymous, reviewer(s) for their contribution to the peer review of this work.

Reprints and permissions information is available at www.nature.com/reprints.

Corresponding author(s):   Jianan Y. Qu

Last updated by author(s):   Apr 21, 2022

Reporting Summary

Nature Research wishes to improve the reproducibility of the work that we publish. This form provides structure for consistency and transparency in reporting. For further information on Nature Research policies, see our Editorial Policies and the Editorial Policy Checklist.

Statistics

For all statistical analyses, confirm that the following items are present in the figure legend, table legend, main text, or Methods section.

n/a	Confirmed	
☐	☒	The exact sample size (*n*) for each experimental group/condition, given as a discrete number and unit of measurement
☒	☐	A statement on whether measurements were taken from distinct samples or whether the same sample was measured repeatedly
☒	☐	The statistical test(s) used AND whether they are one- or two-sided *Only common tests should be described solely by name; describe more complex techniques in the Methods section.*
☒	☐	A description of all covariates tested
☒	☐	A description of any assumptions or corrections, such as tests of normality and adjustment for multiple comparisons
☐	☒	A full description of the statistical parameters including central tendency (e.g. means) or other basic estimates (e.g. regression coefficient) AND variation (e.g. standard deviation) or associated estimates of uncertainty (e.g. confidence intervals)
☒	☐	For null hypothesis testing, the test statistic (e.g. *F*, *t*, *r*) with confidence intervals, effect sizes, degrees of freedom and *P* value noted *Give P values as exact values whenever suitable.*
☒	☐	For Bayesian analysis, information on the choice of priors and Markov chain Monte Carlo settings
☒	☐	For hierarchical and complex designs, identification of the appropriate level for tests and full reporting of outcomes
☒	☐	Estimates of effect sizes (e.g. Cohen's *d*, Pearson's *r*), indicating how they were calculated

Our web collection on statistics for biologists contains articles on many of the points above.

Software and code

Policy information about availability of computer code

Data collection	ScanImage 5.7 running on MATLAB 2019b was used for three-photon imaging data collection. Code written in MATLAB was used to perform direct focus sensing and shaping.
Data analysis	ImageJ 1.52p was used for performing the maximum intensity projection of image stacks, taking line profiles, and for manually selecting regions of interest in the calcium imaging datasets and calculating the Calcium transient within this region. The plugin StackReg (latest version from 16/09/2010) and plugin TurboReg (latest version from 16/09/2010) were used for registration of structural stacks. MATLAB 2019b was used for making plots of laser noise power spectrum density and spatial frequency analysis shown in this Manuscript. Imaris 7.2.1 was used for 3D reconstruction of structural stacks.

For manuscripts utilizing custom algorithms or software that are central to the research but not yet described in published literature, software must be made available to editors and reviewers. We strongly encourage code deposition in a community repository (e.g. GitHub). See the Nature Research guidelines for submitting code & software for further information.

Data

Policy information about availability of data

All manuscripts must include a data availability statement. This statement should provide the following information, where applicable:

- Accession codes, unique identifiers, or web links for publicly available datasets
- A list of figures that have associated raw data
- A description of any restrictions on data availability

The authors declare that the main data supporting the findings of this study are available within the paper, its extended data, and supplementary information files. The Source Data files for all data presented within the Figures and Extended Data can be found at: https://github.com/QuLabHKUST/QuLabAO

Field-specific reporting

Please select the one below that is the best fit for your research. If you are not sure, read the appropriate sections before making your selection.

☒ Life sciences   ☐ Behavioural & social sciences   ☐ Ecological, evolutionary & environmental sciences

For a reference copy of the document with all sections, see nature.com/documents/nr-reporting-summary-flat.pdf

Life sciences study design

All studies must disclose on these points even when the disclosure is negative.

Sample size	For the in vitro experiments (Fig. 1B, E-G, Fig. S3, S4, S12), similar results were obtained on more than 5 measurements. For the in vivo experiments (Fig. 2-5, Fig. S5-11, S13-21, similar measurements were performed on more than 3 mice. The paper is directed to demonstrating a new imaging method for deep in-vivo imaging and did not involve statistical analysis. We showed this method works well for many animals.
Data exclusions	We only excluded data whose quality was compromised by to artifacts, such as defective surgery, low GCaMP6 expression level.
Replication	We performed each imaging experiment on at least 3 different animals with the same age and size to ensure our results are reproducible. All attempts of replication were successful in this study.
Randomization	There is no group allocated in this study.
Blinding	Blinding was not relevant to this study because we had no knowledge of the results before the collection and analyses of the raw data.

Reporting for specific materials, systems and methods

We require information from authors about some types of materials, experimental systems and methods used in many studies. Here, indicate whether each material, system or method listed is relevant to your study. If you are not sure if a list item applies to your research, read the appropriate section before selecting a response.

Materials & experimental systems

n/a	Involved in the study
☒	☐ Antibodies
☒	☐ Eukaryotic cell lines
☒	☐ Palaeontology and archaeology
☐	☒ Animals and other organisms
☒	☐ Human research participants
☒	☐ Clinical data
☒	☐ Dual use research of concern

Methods

n/a	Involved in the study
☒	☐ ChIP-seq
☒	☐ Flow cytometry
☒	☐ MRI-based neuroimaging

Animals and other organisms

Policy information about studies involving animals; ARRIVE guidelines recommended for reporting animal research

Laboratory animals	Both males and females are included in this study. The animals are kept under an environment temperature of 26 to 28 celsius degree and 12 light/12 dark cycle. The humidity is 40% to 60%.
Wild animals	No wild animals were involved in this study.
Field-collected samples	No field -collected samples were involved in this study.

Ethics oversight | All animal procedures were conducted in accordance with the Guidelines of the Animal Care Facility of the Hong Kong University of Science and Technology (HKUST) and have been approved by the Animal Ethics Committee at HKUST

Note that full information on the approval of the study protocol must also be provided in the manuscript.